1

Mario Nachbar[1], Denis Duft[2], Alexei Kiselev[2] and Thomas Leisner[1,2]

Composition, mixing state and water affinity of meteoric smoke analogue nanoparticles produced in a non-thermal microwave plasma source

MSP analogues produced in a microwave plasma resonator

[1]Institute of Environmental Physics, University of Heidelberg, Im Neuenheimer Feld 229, 69120 Heidelberg, Germany
[2]Institute of Meteorology and Climate Research, Karlsruhe Institute of Technology – KIT, Hermann-von-Helmholtz-Platz 1, 76344 Eggenstein-Leopoldshafen, Germany

Corresponding author: Mario Nachbar (address: Hermann-von-Helmholtz-Platz 1, 76344 Eggenstein-Leopoldshafen, Germany; phone: +4972160829074; e-mail: mario.nachbar@kit.edu)

Abstract: The article reports on the composition, mixing state and water affinity of iron silicate particles which were produced in a non-thermal low-pressure microwave plasma reactor. The particles are intended to be used as meteoric smoke particle analogues. We used the organometallic precursors ferrocene ($Fe(C_5H_5)_2$) and tetraethyl orthosilicate (TEOS, $Si(OC_2H_5)_4$) in various mixing ratios to produce nanoparticles with radii between 1 nm and 4 nm. The nanoparticles were deposited on sample grids and their stoichiometric composition was analyzed in an electron microscope using energy dispersive X-ray spectroscopy (EDS). We show that the pure silicon oxide and iron oxide particles consist of SiO_2 and Fe_2O_3, respectively. For Fe:(Fe+Si) ratios between 0.2 and 0.8 our reactor produces (in contrast to other particle sources) mixed iron silicates with a stoichiometric composition according to $Fe_xSi_{(1-x)}O_3$ ($0 \leq x \leq 1$). This indicates that the particles are formed by polymerization of FeO_3 and SiO_3 and that rearrangement to the more stable silicates ferrosilite ($FeSiO_3$) and fayalite (Fe_2SiO_4) does not occur at these conditions. To investigate the internal mixing state of the particles, the H_2O surface desorption energy of the particles was measured. We found that the nanoparticles are internally mixed and that differential coating resulting in a core-shell structure does not occur.

Keywords: Microwave Plasma, Nanoparticles, EDS, Meteoric Smoke Particles, Iron Silicates

1 Introduction

Nanoparticles are of great importance for many chemical and physical applications and research fields. In planetary atmospheres, they serve as important condensation nuclei triggering the formation of clouds: Every day, about 40 tons of meteoric material enters the atmosphere of Earth (1, 2). This material ablates in the upper atmosphere with peak ablation heights of the major elemental components Fe, Si and Mg at a height between 80 km and 90 km (3). Oxides, carbonates and hydroxides are formed via oxidation by O_3, O_2, CO_2 and H_2O and then serve as building blocks for so called Meteoric Smoke Particles (MSP) (4). In the summer mesopause in Earth's atmosphere, the majority of MSPs is smaller than 2 nm in radius (5-10) and they are believed to serve as nuclei for the formation of noctilucent clouds (NLCs) (10-12). On Mars, the peak meteoric ablation height is between 60 km and 100 km (13-15), which is consistent with heights of CO_2 cloud observations (16-21) adverting the importance of MSPs as potential condensation nuclei. Indeed, Listowski and co-workers were only able to model realistic Martian mesospheric cloud patterns when assuming the presence of MSPs (22).

Due the small size of MSPs it is a challenging task to measure the MSP concentration and composition in the mesosphere which is subject of ongoing research. Current investigations point to an iron rich chemical formula (11, 23). Analogue materials for various kinds of cosmic dust have been produced by vapor condensation, sol-gel preparation or photo-oxidation (24-26). These methods do not mimic realistic conditions at which particles are formed in planetary atmospheres or the interstellar medium, but are used to produce particles with chemical compositions they might consist of. Here, we present a method to produce MSP analogues of realistic size using a non-thermal low-pressure mi-

crowave plasma reactor. This method does not mimic realistic conditions at which MSPs are produced in the atmosphere as well, but allows creating particles which consist of the major elements expected to be in MSPs. These particles thus serve as MSP analogues and are used to study cloud formation processes at realistic mesospheric conditions of Mars and Earth with the recently introduced MICE-TRAPS setup (27, 28).

Understanding mesospheric cloud formation requires nucleation experiments conducted with the complete composition range of MSPs, since the nucleation ability of the particles is likely to be material dependent. In addition, MSPs might heat up in the low pressure environment of the mesosphere by absorption of sunlight (29). The absorption ability of the particles is material dependent and is studied in ongoing research.

In this work, we characterize mixed iron silicate nanoparticles produced in a non-thermal low pressure microwave plasma reactor. The paper is organized as follows: In section 2, we introduce the used experimental techniques which are Energy Dispersive Spectroscopy (EDS) and H_2O adsorption measurements with MICE-TRAPS. We show in section 3 that pure iron oxide and silicon oxide particles are composed of Fe_2O_3 and SiO_2, respectively. Mixed iron-silicate particles, however, are composed of a homogeneous mix of FeO_3 and SiO_3 molecules with their ratio being controlled by the iron and silicon concentration in the plasma reactor. We conclude with a summary of the results and an outlook in section 4.

2 Experimental

2.1 Nanoparticle generation

Metal oxide nanoparticles were produced in a non-thermal low-pressure (60 mbar) microwave plasma reactor. The operating principle of such nanoparticle sources has been described previously in detail (e.g. 30). The shape of metal oxide nanoparticles produced in similar experimental setups has been shown to be compact and spherical with a marginal degree of agglomeration (31-34). The design of the nanoparticle source employed in this experiment is depicted schematically in Figure 1. Compared to other designs of this type the setup differs in the way of precursor vaporization and mixing with the background gas flow which we will describe in more detail. Organometallic precursors are stored in separate and independently temperature-controlled reservoirs. The amount of precursor vapor added to the background flow in the mixer is determined solely by the temperature of the precursor reservoir. This setup has the advantages that it is very simple and that liquid and solid precursors can be vaporized using identical reservoirs without the need for additional flow controlled gas lines. In this study we use tetraethyl orthosilicate (TEOS, $Si(OC_2H_5)_4$, Sigma Aldrich) and ferrocene ($Fe(C_5H_5)_2$, Sigma Aldrich) as precursors for silicon and iron, respectively. The precursor vapors are mixed with a continuous 3 slpm flow of Helium to which a 100 sccm flow of O_2 is added downstream. The addition of O_2 is processed behind an orifice in flow direction to avoid premature oxidization and deposition of the low volatile metal oxides, which has been observed to occur for some precursors. Pressure and flow conditions ensure diffusive mixing of vapors and gases within a few centimeters. After mixing, the flow enters a quartz glass tube of 2.2 cm inner diameter and 40 cm length. The Reynolds number of the flow in this tube of Re~24 indicates a laminar regime. The tube is placed in the center of the microwave resonator at which a microwave induced plasma of about 15 cm length is ignited (2.45 GHz, 350 W). The flow rate results in a retention time of about 60 ms in the plasma during which the precursor molecules completely decompose causing the release of Fe and Si atoms. The presence of oxygen (3 mol%) in the gas flow assures oxidization of these atoms which then form particles. In addition, the organic parts of the precursors are efficiently oxidized to volatile carbon dioxide and water which are not included in the particle material. A precursor mixing ratio of 30 ppm (0.003 mol%) or less was maintained in the reactor cell such that the ratio of O_2 per precursor molecule was always at or higher than 1000. For comparison, to oxidize the organic parts of TEOS and ferrocene molecules requires 11 and 12.5 molecules of O_2, respectively. The bulk of the particle-laden flow behind the discharge region is pumped off and discarded and less than 20% of the sample flow is extracted and fed to the nanoparticle characterization unit.
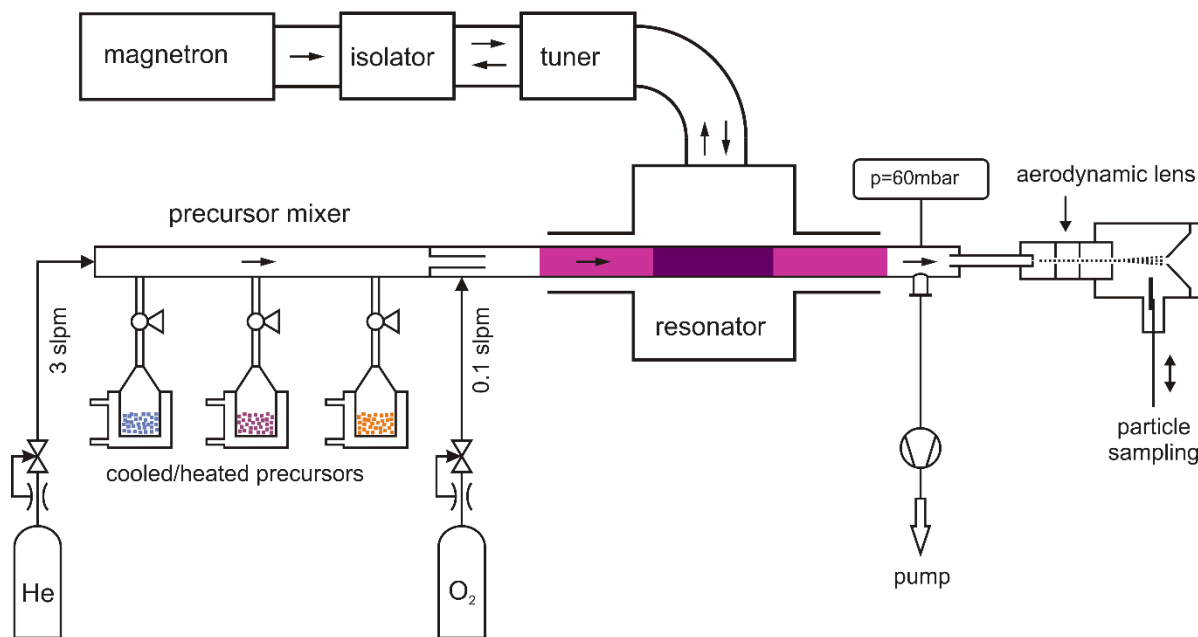
Fig. 1: Schematic representation of the microwave plasma nanoparticle source.

To study nanoparticle properties using the MICE-TRAPS apparatus the nanoparticles were separated from the residual gas of the nanoparticle source using an aerodynamic lens (ADL) and a differential pumping stage which has been described in detail previously (28). After the ADL, the particle beam enters the main vacuum chamber through a skimmer. At this point, a target plate was inserted to deposit the particles on standard transmission electron microscope (TEM) sample grids (Ø 3mm, copper mesh, coated with carbon film). The particle mass distribution at the output of the nanoparticle source depends on pressure, flow conditions, precursor concentration in the plasma reactor and retention time. It was found, that for the conditions employed in this experiment using only a single precursor, particles with diameter ranging from 2 to 8 nm were produced. The charge state of the particles depends on various parameters such as precursor composition and concentration, microwave power, retention time and other parameters of the microwave induced plasma. Although the exact particle charge distribution could not be measured, we assume that about 50% of the particles are neutral and 50% are singly charged with a preference towards carrying a positive charge. The exact values, however, may differ substantially depending on the above mentioned parameters.

2.2 Nanoparticle composition

After particle deposition, the TEM sample grids were analyzed in a scanning electron microscope (SEM, FEI Quanta 650 FEG) using an energy dispersive X-ray spectrometer (EDS, Bruker Quantax XFlash 5010). The sample grids loaded with nanoparticles were placed perpendicular to the electron beam. EDS spectra were obtained with a 10 keV beam scanning a square area size of 200x200μm on the sample surface. Exemplary SEM images and EDS spectra of a bare TEM grid (a) and a grid with iron-silicate particle deposit (b) are shown in Fig. 2 for photon energies between 0.1keV and 2keV. The insert in the lower right part shows the EDS spectra of the iron-silicate particle deposit for photon energies between 5 keV and 7 keV. The EDS spectrum of the bare grid shows the characteristic peaks associated with the copper bulk material of the grid (L-line, 0.93 keV). The spectrum also shows weak peaks of C (K-line, 0.277 keV) and O which are always observed by the EDS detector in this instrument independent of the sample. The EDS spectrum of an iron silicate deposit shows peaks which are attributed to the presence of O (K-line, 0.525 keV), Fe (L-line, 0.705 keV) and Si (K-line, 1.74 keV). The carbon peak in the EDS spectra of the iron silicate deposit is only slightly increased compared to the bare grid. This confirms that no eminent amount of carbon is present in the particle material.
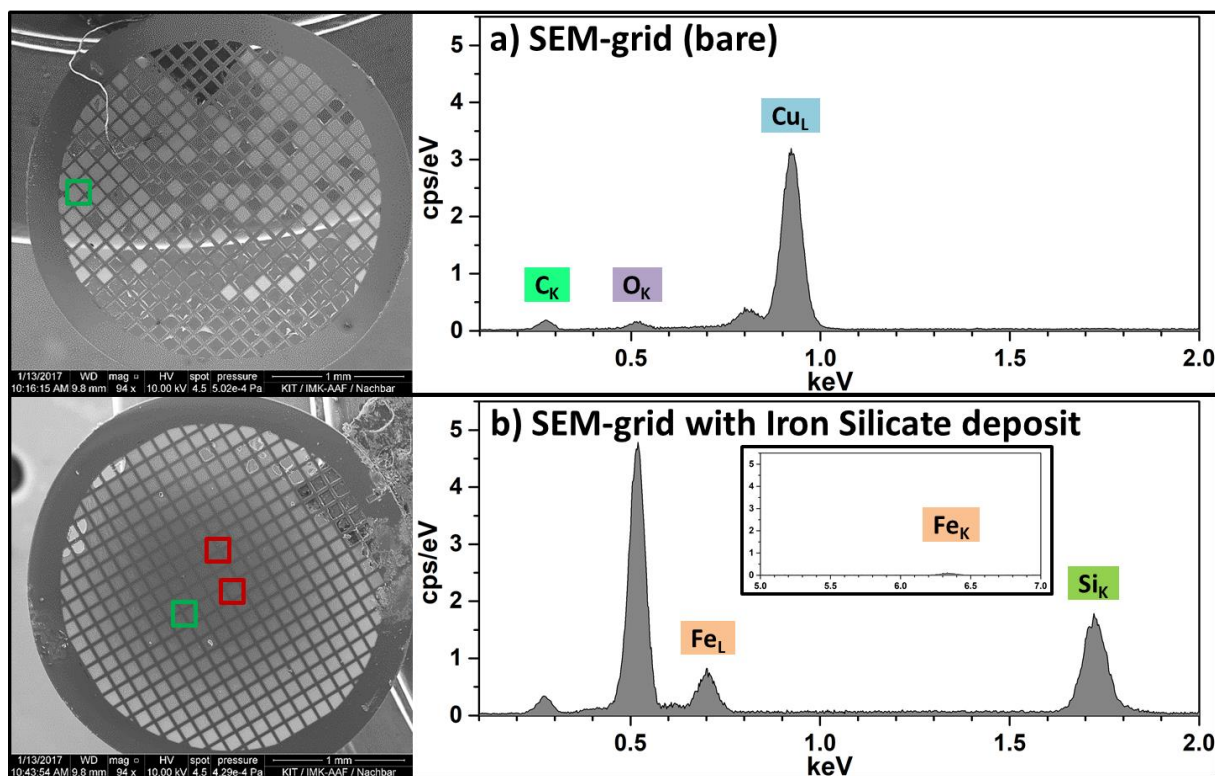
Fig. 2: Left panels: SEM images of a bare grid (a, top) and of a grid covered with iron-silicate nanoparticles (b, bottom) (scale bar 1 mm). Right panels: EDS spectra taken at the electron beam scanning locations indicated by the green boxes in the SEM images. Horizontal axis is photon energy (0.1 to 2keV) and vertical axis is photon count rate (0 to 5.5 cps/eV bin). Positions of the main emission peaks of C, O, Fe, Cu, and Si are labeled. The insert shows the high energy part of the spectrum (5 to 7keV) using the same vertical scale and illustrates the intensity of the Fe_K-line at low iron content.

Quantitative analysis of the elemental composition was performed using the Esprit 1.9 software by Bruker. The analysis employed in the software is based on evaluating the peak to background ratios which are then input to a modified ZAF matrix correction which accounts for atomic number (Z), absorption (A) and secondary fluorescence effects (F). A detailed description of the method can be found in (35-37). Data was only obtained for thick deposit layers, so that no copper signal from the TEM grid is present in the EDS spectra. At 10 keV excitation energy the Fe_K-line and Fe_L-line can be used for quantitative analysis. In general, analysis of the Fe_K-line usually provides more accurate results than the Fe_L-line as interference with the overlapping O_K-line and additional errors occurring due to a higher background and varying absorption effects in the low energy range can be avoided. However, for samples with a low iron content as presented in panel b) of Fig. 2 (Fe:(Fe+Si)=0.38) the intensity of the Fe_K-line (6.405keV) was so low (cf. insert) that analyzing the Fe_L-line resulted in a lower uncertainty determined by the analysis software. For analysis of the iron content we always used the line resulting in the lower uncertainty. For each sample, EDS spectra were taken at three different scanning locations. It was found that for all samples the variance of analyzed elemental composition between each location was smaller than the uncertainty given by the analysis software for a single spectrum. Thus, we assume that the result is independent from the chosen scanning location.

2.3 Nanoparticle mixing state

To study the particle mixing state, the nanoparticle surface was investigated by measuring the desorption energy of water molecules with the MICE-TRAPS apparatus. The device (38) and the method using CO_2 as the adsorbent (39) have been described in previous publications. In this work, H_2O has been used as the adsorbent. In brief, the nanoparticles are mass selected and trapped in MICE and are exposed to a flux of water molecules at a temperature of about 145K. Under such conditions the initially bare particle surface adsorbs water molecules until an equilibrium surface concentration is reached. The adsorption equilibrium is determined by the ratio of adsorption and desorption rate where the latter is described by the H_2O desorption energy, a surface property characteristic for the nanoparticle material. The desorption energy is expected to reflect the chemical composition of the nanoparticle surface and provides indications on the internal particle mixing state. The adsorption pro-

cess is monitored by measuring the particle mass with a time-of-flight mass spectrometer (TOF-MS) at regular time intervals. This is achieved by extracting small samples of the trapped particle cloud from MICE through the electrostatic exit lens of the ion trap and guiding the particles into the acceleration zone of the TOF-MS. The left panel of Fig. 3 shows exemplary measurements of the particle mass as a function of the trapping time in MICE for pure iron oxide and silica nanoparticles.
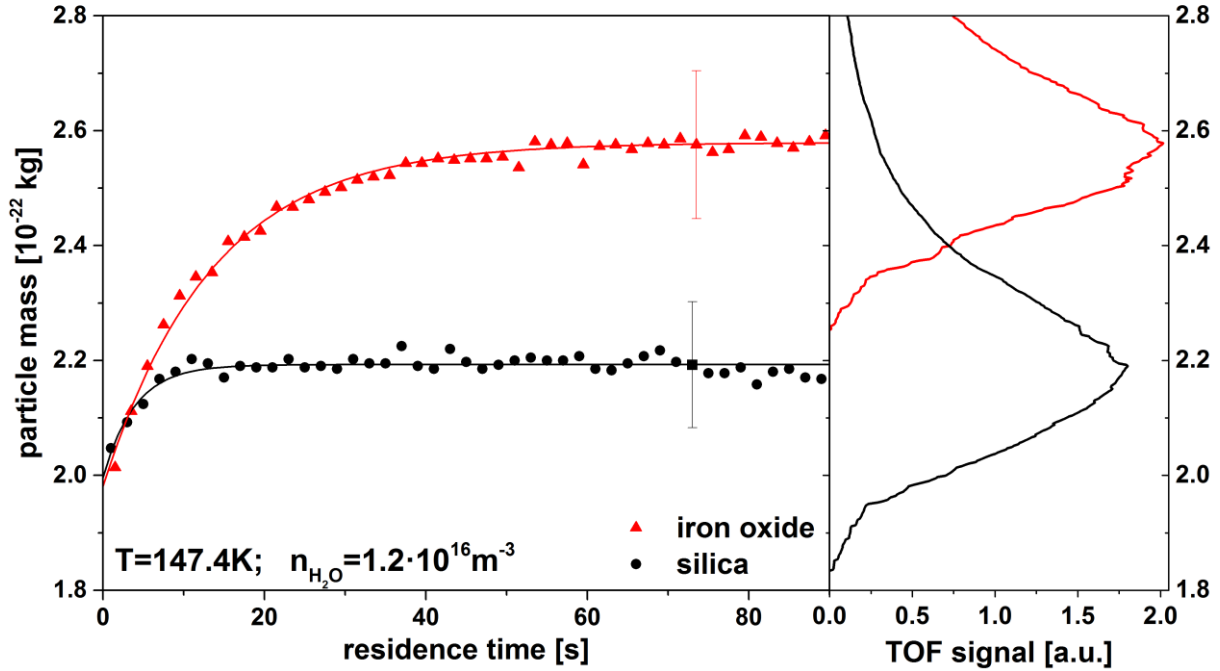
Fig. 3: Left panel: Nanoparticle mass during H_2O adsorption process as function of the residence time in MICE for iron oxide (red triangles) and silica (black dots) nanoparticles with initial mass $m_0 = 2 \cdot 10^{-22}$kg. The solid lines are exponential decay fits to determine the adsorbed water mass for each measurement. Right panel: Smoothed time-of-flight mass spectra for two selected points marked with error bars in the left panel at t=73s. The particle mass is shown as a function of the TOF signal. The position of the peak maximum is used as the mean particle mass plotted in the left panel.

Starting with an initial mass of $m_0 = 2 \cdot 10^{-22}$ kg (=$1.2 \cdot 10^5$ u) for both materials the particles adsorb water vapor and quickly reach an equilibrium state. Iron oxide exhibits a higher desorption energy than silica and adsorbs more water on the particle surface. The mass of adsorbed water m_{ads} is determined from the measurement by fitting a single exponential decay of the form $m(t) = m_0 + m_{ads}\left(1 - e^{-t/\tau}\right)$ to the data. The adsorbed water mass relates to the desorption energy F_{des} by the following equation (40):

$$m_{ads} = \frac{n_{H2O} \cdot A_0}{f_{vib}\sqrt{2\pi}} \cdot \sqrt{m_{H2O}kT} \cdot \exp\left(\frac{F_{des}}{kT}\right) \tag{1}$$

Here, n_{H2O} is the water vapor density in MICE, m_{H2O} is the mass of a water molecule, k is the Boltzmann constant, T is the temperature, f_{vib} is the vibrational frequency (10^{13} Hz for H_2O), and $A_0 = \left(6\sqrt{\pi}\, m_0/\varrho\right)^{2/3}$ is the initial particle surface area which is calculated from the initial particle mass m_0 and particle density ϱ assuming spherical particles. For iron-silicates of various compositions no tabulated values for the bulk densities are available. We assume a density that is a linear combination of the densities of iron oxide ($\varrho \sim 5.2$g/cm³) and silica ($\varrho \sim 2.3$g/cm³) according to the elemental ratio of iron to silicon. Equation (1) can be rearranged to yield the desorption energy as function of particle size and adsorbed water mass.

The data points in the left panel of Fig. 3 were obtained from the peak position of the time-of-flight mass spectra shown in the right panel exemplary for the two data points marked with error bars. The width of the peaks is specific for the TOF instrument and detector design. The width of the particle mass distribution trapped in MICE is typically much smaller. The peak position, however, is a very precise indicator of the mean particles mass. The difference in adsorbed water mass between both particle materials can easily be resolved.

To investigate the particle mixing state we analyze F_{des} as function of particle composition determined from EDS. For mixed particles containing both Fe and Si, we consider three possible scenarios: 1: Two independent classes of particles are produced in the particle source, one pure Fe-containing and one pure Si-containing class. 2: The particles created in the particle source exhibit a core-shell structure, where the core contains only one metal oxide which is then covered with a shell of the other metal oxide. This scenario could be realized if differential break-up of the precursors occurs in the flow reactor. 3: The particles are completely internally mixed, i.e. the chemical composition at the surface and in the bulk are identical. For case 1 the mass spectra for mixed particles should exhibit two distinct peaks, as both particle classes would adsorb water according to the measurements shown in Fig. 3. For case 2 the spectra should exhibit one distinct peak with the desorption energy being the same as either pure Fe- or pure Si-oxide particles. For case 3 one distinct TOF peak resulting in an intermediate value for the desorption energy would be anticipated. While changing the Fe content of the particles a continuous transition of the desorption energy from pure Si to pure Fe oxide would be expected.

3 Results and Discussion

3.1 EDS analysis

Mixed iron silicates were produced by varying the temperature of the precursors. For TEOS, temperatures were varied between 2°C and 30°C and for Ferrocene between 45°C and 90°C. The particles were deposited on sample grids whereupon the iron, silicon and oxygen content was analyzed using EDS. The iron to silicon ratio of the particle material was proportional to the vapor pressure ratio of both precursors at the applied temperatures. Fig. 4 shows the element to oxygen ratio for iron and silicon containing nanoparticles produced in the microwave nanoparticle source and analyzed using EDS as described above.
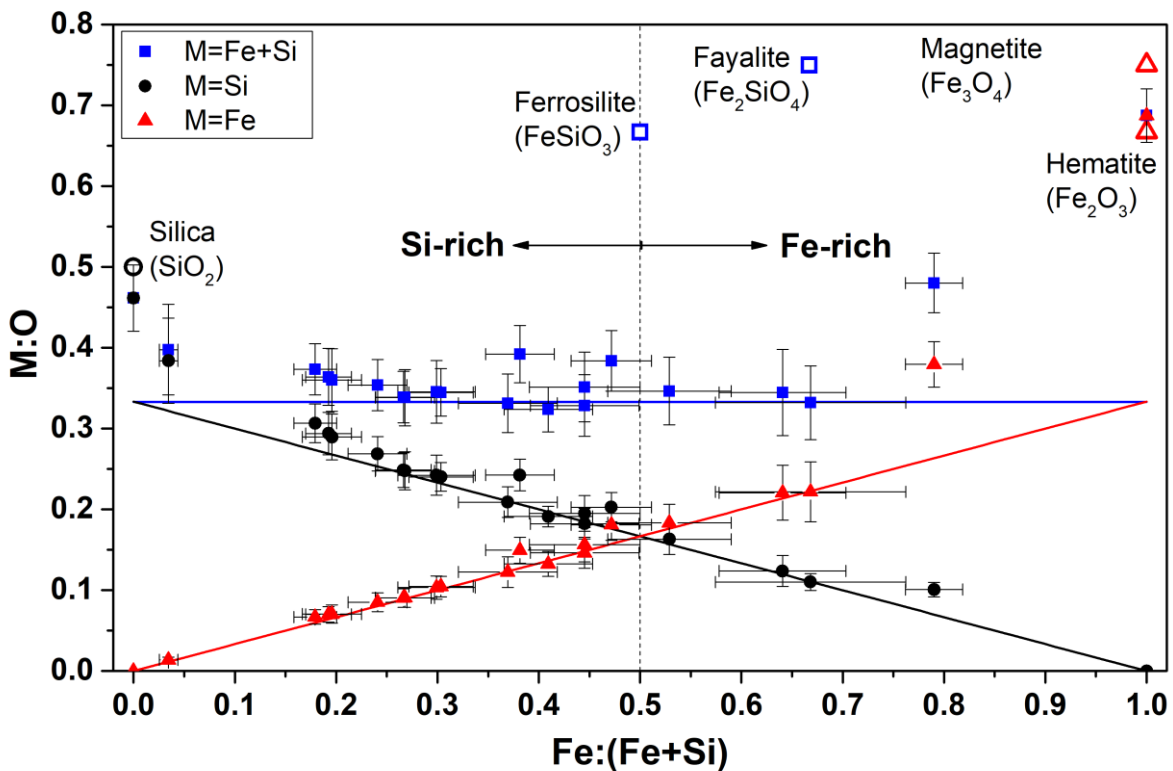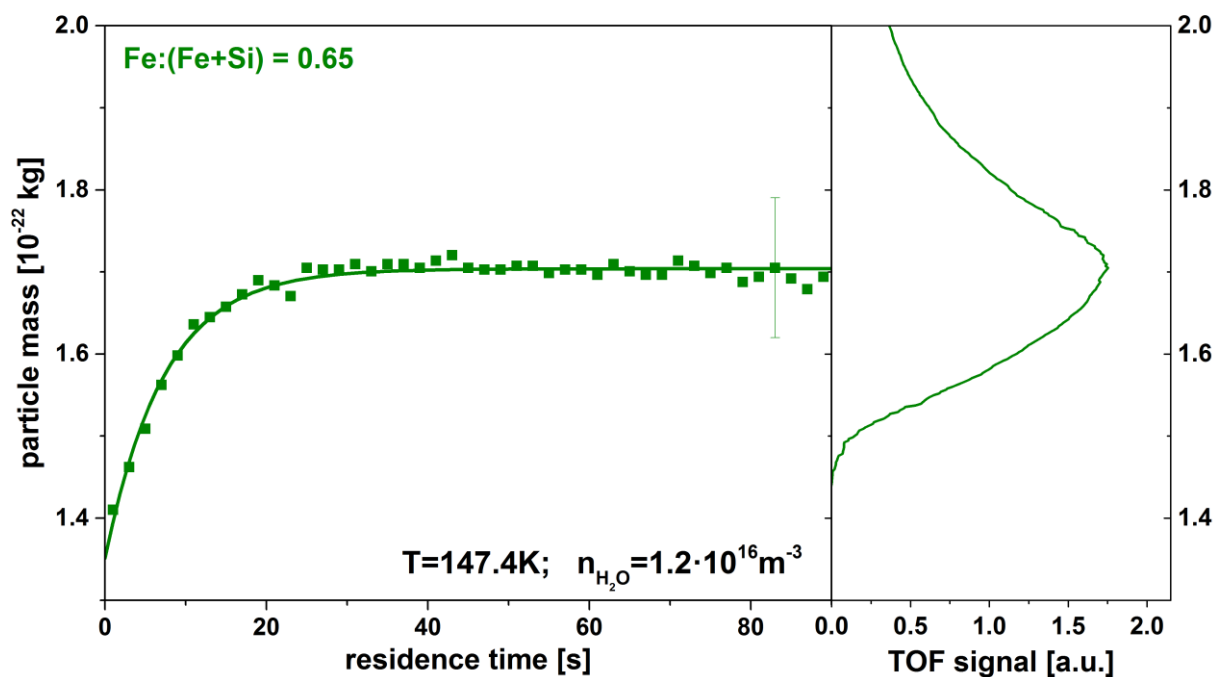

Fig. 4: Element to oxygen ratio M:O of iron-silicate nanoparticles plotted against the relative content of Fe. Open symbols indicate elemental ratios of natural iron and silicate minerals.

The relative abundances of Fe (red triangles), Si (black dots) and Fe+Si combined (blue squares) with respect to oxygen against the relative Fe content in the particles are shown. Additionally, the plot con-

tains the relative abundances of Fe, Si, and Fe+Si for the natural occurring minerals silica (SiO_2), magnetite (Fe_3O_4), hematite (Fe_2O_3), ferrosilite ($FeSiO_3$), and fayalite (Fe_2SiO_4) according to their theoretical stoichiometric composition shown as open symbols. At zero iron content, the nanoparticle composition coincides with the composition of silica, which agrees with a previous finding in a similar experimental arrangement (41). At zero silicon content, the nanoparticle composition matches the iron to oxygen ratio of Fe_2O_3. This compares well with studies in which microwave plasma particle sources were used to produce iron oxide nanoparticles and which identified the particle material as Fe_2O_3 using XRD, Raman spectroscopy and Mössbauer spectroscopy (42, 43). At intermediate iron content (0.2 < Fe:(Fe+Si) < 0.8), the particle composition does not show a linear transition between SiO_2 and Fe_2O_3. Instead, the particle composition follows a lower M:O ratio and Fe appears to be continuously interchangeable with Si. In fact, the measured composition is well represented by the system $Fe_xSi_{(1-x)}O_3$ ($0 \leq x \leq 1$) which is plotted in Fig 4 as solid lines. The continuous exchange of Fe and Si indicates that the particle formation occurs by polymerization of gas phase FeO_3 and SiO_3. In contrast to the production of iron oxide and silica particles, further rearrangement to more stable silicates does not occur. In addition, we observed a 10 to 100 times higher particle mass production rate when mixed iron silicates were produced compared to only using one precursor material. These observations show that the chemistry involved in particle formation is altered when producing mixed iron silicates. Photooxidization in the presence of O_2 and O_3 at room temperature and atmospheric pressure has shown to produce a different particle material (25, 26): Here, independent of the applied gas phase concentrations of the iron and silicon precursors, only an iron to silicon ratio of 2 was produced. This reaction product corresponds to the mineral fayalite (Fe_2SiO_4) and indicates a different reaction pathway.

However, the composition as determined by EDS does not necessarily reflect the composition of individual particles as the scan area of the electron beam (200x200µm) always covers many deposited nanoparticles. The EDS results are an average of the composition of the particles deposited on the sample grids. To elucidate the particle mixing state, additional information was provided by measuring the surface sensitive adsorption and desorption of H_2O on the nanoparticles.
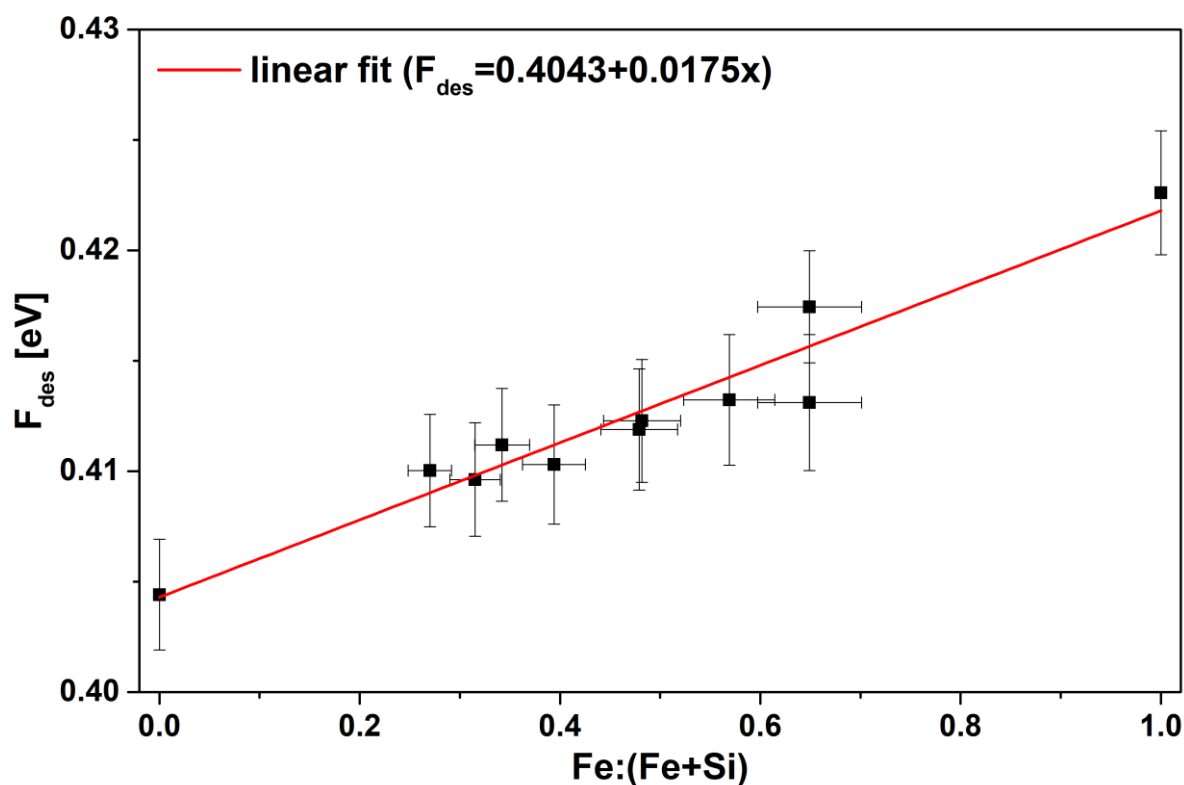
3.2 H_2O desorption energy

The water vapor surface desorption energy of oxide nanoparticles with varying Fe and Si content has been measured using the method described above. One example measurement is shown in the left panel of Fig. 5 for a mixing ratio of Fe:(Fe+Si) = 0.65.

Fig. 5: Left panel: Nanoparticle mass against residence time in MICE for mixed iron and silicon containing particles. Right panel: Smoothed TOF mass spectrum corresponding to the point marked with error bars at t=83s.

The right panel depicts the TOF spectrum corresponding to the single data point marked with error bars at t=83 s residence time. The TOF spectrum shows a single peak only with a peak width which is identical to the peak width for pure nanoparticles. As we have argued above, this indicates that all particles of the trapped particle population indeed adsorb the same amount of water molecules and thus have the same desorption energy. This finding eliminates the possibility of two or more particle classes with different desorption energies present in the trapped particle cloud.

To further investigate the particle mixing state, a series of desorption energy measurements were performed with particles of 2 nm in radius and varying Fe:(Fe+Si) particle mixing ratios and the results are shown in Fig. 6. The data shows a linear transition of the desorption energy from pure silica to pure iron-oxide particles. This indicates that the surface composition also follows a smooth transition and that the stoichiometric composition which has been determined by EDS measurements directly reflects the surface properties of the nanoparticles. We conclude that the nanoparticles are completely internally mixed and that differential coating to a core-shell structure does not occur.

Fig. 6: H_2O desorption energy for nanoparticles (r = 2nm ± 0.2nm) of varying Fe and Si content. The solid line represents a linear fit to the data.

4 Summary and Outlook

In this study, we characterized the composition of MSP analogue nanoparticles produced in a non-thermal low-pressure microwave plasma source. EDS measurements show that silicon oxide particles consist of silica (SiO_2) and iron oxide particles are composed of Fe_2O_3. In addition, mixed iron silicates with an Fe:(Fe+Si) ratio between 0.2 and 0.8 are present in the form of $Fe_xSi_{(1-x)}O_3$ ($0 \leq x \leq 1$) with the ratio of Fe to Si molecules reflecting the iron and silicon molecule concentration in the plasma reactor. H_2O adsorption measurements using MICE-TRAPS were used to conclude that only one particle class is produced, that the nanoparticles are internally mixed and that differential coating to a core-shell structure does not occur. In future work, we will add a magnesium precursor to the system and study the composition of mixed magnesium-iron-silicates. Measurements of the material dependent light absorption coefficient of these now well characterized particles as well as their H_2O nucleation ability will be part of upcoming publications.

Bibliography

1. Carrillo-Sanchez JD, Nesvorny D, Pokorny P, Janches D, & Plane JMC (2016) Sources of cosmic dust in the Earth's atmosphere. *Geophys. Res. Lett.* 43(23):11979-11986.
2. Plane JMC (2012) Cosmic dust in the earth's atmosphere. *Chem. Soc. Rev.* 41(19):6507-6518.
3. Vondrak T, Plane JMC, Broadley S, & Janches D (2008) A chemical model of meteoric ablation. *Atmospheric Chemistry and Physics* 8(23):7015-7031.
4. Plane JMC, Feng W, & Dawkins ECM (2015) The Mesosphere and Metals: Chemistry and Changes. *Chemical Reviews* 115(10):4497-4541.
5. Bardeen CG, Toon OB, Jensen EJ, Marsh DR, & Harvey VL (2008) Numerical simulations of the three-dimensional distribution of meteoric dust in the mesosphere and upper stratosphere. *J. Geophys. Res.-Atmos.* 113(D17).
6. Megner L, Rapp M, & Gumbel J (2006) Distribution of meteoric smoke - sensitivity to microphysical properties and atmospheric conditions. *Atmos. Chem. Phys.* 6:4415-4426.
7. Megner L, Siskind DE, Rapp M, & Gumbel J (2008) Global and temporal distribution of meteoric smoke: A two-dimensional simulation study. *J. Geophys. Res.-Atmos.* 113(D3):15.
8. Hunten DM, Turco RP, & Toon OB (1980) Smoke And Dust Particles Of Meteoric Origin In The Mesosphere And Stratosphere. *J. Atmos. Sci.* 37(6):1342-1357.
9. Megner L, Gumbel J, Rapp M, & Siskind DE (2008) Reduced meteoric smoke particle density at the summer pole - Implications for mesospheric ice particle nucleation. *Adv. Space Res.* 41(1):41-49.
10. Havnes O, Gumbel J, Antonsen T, Hedin J, & La Hoz C (2014) On the size distribution of collision fragments of NLC dust particles and their relevance to meteoric smoke particles. *J. Atmos. Sol.-Terr. Phys.* 118:190-198.
11. Hervig ME, *et al.* (2012) The content and composition of meteoric smoke in mesospheric ice particles from SOFIE observations. *J. Atmos. Sol.-Terr. Phys.* 84-85:1-6.
12. Rapp M & Thomas GE (2006) Modeling the microphysics of mesospheric ice particles: Assessment of current capabilities and basic sensitivities. *J. Atmos. Sol.-Terr. Phys.* 68(7):715-744.
13. Adolfsson LG, Gustafson BAS, & Murray CD (1996) The Martian atmosphere as a meteoroid detector. *Icarus* 119(1):144-152.
14. Whalley CL & Plane JMC (2010) Meteoric ion layers in the Martian atmosphere. *Faraday Discuss.* 147:349-368.
15. Crismani MMJ, *et al.* (2017) Detection of a persistent meteoric metal layer in the Martian atmosphere. *Nat. Geosci.* 10(6):401-+.
16. Montmessin F, *et al.* (2006) Subvisible CO2 ice clouds detected in the mesosphere of Mars. *Icarus* 183(2):403-410.
17. Vincendon M, Pilorget C, Gondet B, Murchie S, & Bibring JP (2011) New near-IR observations of mesospheric CO2 and H2O clouds on Mars. *Journal of Geophysical Research-Planets* 116:18.
18. Montmessin F, *et al.* (2007) Hyperspectral imaging of convective CO2 ice clouds in the equatorial mesosphere of Mars. *J. Geophys. Res.-Planets* 112(E11).
19. Määttänen A, *et al.* (2010) Mapping the mesospheric CO2 clouds on Mars: MEx/OMEGA and MEx/HRSC observations and challenges for atmospheric models. *Icarus* 209(2):452-469.
20. Clancy RT, Wolff MJ, Whitney BA, Cantor BA, & Smith MD (2007) Mars equatorial mesospheric clouds: Global occurrence and physical properties from Mars Global Surveyor Thermal Emission Spectrometer and Mars Orbiter Camera limb observations. *J. Geophys. Res.-Planets* 112(E4).
21. Stevens MH, *et al.* (2017) Martian mesospheric cloud observations by IUVS on MAVEN: Thermal tides coupled to the upper atmosphere. *Geophys. Res. Lett.* 44(10):4709-4715.
22. Listowski C, Maattanen A, Montmessin F, Spiga A, & Lefevre F (2014) Modeling the microphysics of CO2 ice clouds within wave-induced cold pockets in the martian mesosphere. *Icarus* 237:239-261.
23. Rapp M, *et al.* (2012) In situ observations of meteor smoke particles (MSP) during the Geminids 2010: constraints on MSP size, work function and composition. *Ann. Geophys.* 30(12):1661-1673.
24. Colangeli L, *et al.* (2003) The role of laboratory experiments in the characterisation of silicon-based cosmic material. *Astron. Astrophys. Rev.* 11(2-3):97-152.
25. Saunders RW & Plane JMC (2006) A laboratory study of meteor smoke analogues: Composition, optical properties and growth kinetics. *J. Atmos. Sol.-Terr. Phys.* 68(18):2182-2202.
26. Saunders RW & Plane JMC (2011) A photo-chemical method for the production of olivine nanoparticles as cosmic dust analogues. *Icarus* 212(1):373-382.
27. Duft D, Nachbar M, Eritt M, & Leisner T (2015) A Linear Trap for Studying the Interaction of Nanoparticles with Supersaturated Vapors. *Aerosol Sci. Technol.* 49(9):683-691.

28. Meinen J, Khasminskaya S, Ruhl E, Baumann W, & Leisner T (2010) The TRAPS Apparatus: Enhancing Target Density of Nanoparticle Beams in Vacuum for X-ray and Optical Spectroscopy. *Aerosol Science and Technology* 44(4):316-328.

29. Asmus H, Wilms H, Strelnikov B, & Rapp M (2014) On the heterogeneous nucleation of mesospheric ice on meteoric smoke particles: Microphysical modeling. *J. Atmos. Sol.-Terr. Phys.* 118:180-189.

30. Szabó D & Schlabach S (2014) Microwave Plasma Synthesis of Materials—From Physics and Chemistry to Nanoparticles: A Materials Scientist's Viewpoint. *Inorganics* 2(3):468.

31. Baumann W, Thedekar B-S, Paur H-R, & Seifert H (2006) Characterization of Nanoparticles Synthesized in the Microwave Plasma Discharge Process by Particle Mass Spectrometry and Transmission Electron Microscopy. in *AIChE Annual Meeting* (San Francisco).

32. Giesen B, Wiggers H, Kowalik A, & Roth P (2005) Formation of Si-nanoparticles in a microwave reactor: Comparison between experiments and modelling. *J. Nanopart. Res.* 7(1):29-41.

33. Janzen C, Kleinwechter H, Knipping J, Wiggers H, & Roth P (2002) Size analysis in low-pressure nanoparticle reactors: comparison of particle mass spectrometry with in situ probing transmission electron microscopy. *J. Aerosol. Sci.* 33(6):833-841.

34. Nadeem K*, et al.* (2012) Spin-glass freezing of maghemite nanoparticles prepared by microwave plasma synthesis. *J. Appl. Phys.* 111(11):6.

35. Heckel J & Jugelt P (1984) QUANTITATIVE-ANALYSIS OF BULK SAMPLES WITHOUT STANDARDS BY USING PEAK-TO-BACKGROUND RATIOS. *X-Ray Spectrom.* 13(4):159-165.

36. Trincavelli J & Vangrieken R (1994) PEAK-TO-BACKGROUND METHOD FOR STANDARDLESS ELECTRON-MICROPROBE ANALYSIS OF PARTICLES. *X-Ray Spectrom.* 23(6):254-260.

37. Trincavelli J, Limandri S, & Bonetto R (2014) Standardless quantification methods in electron probe microanalysis. *Spectroc. Acta Pt. B-Atom. Spectr.* 101:76-85.

38. Duft D, Nachbar M, Eritt M, & Leisner T (2015) A Linear Trap for Studying the Interaction of Nanoparticles with Supersaturated Vapors. *Aerosol Science and Technology* 49(9):682-690.

39. Nachbar M*, et al.* (2016) Laboratory measurements of heterogeneous CO2 ice nucleation on nanoparticles under conditions relevant to the Martian mesosphere. *Journal of Geophysical Research-Planets* 121(5):753-769.

40. Pruppacher HR & Klett JD (1997) *Microphysics of Clouds and Precipitation* (Kluwer Academic Publishers, Dordrecht).

41. Knipping J*, et al.* (2004) Synthesis of high purity silicon nanoparticles in a low pressure microwave reactor. *J. Nanosci. Nanotechnol.* 4(8):1039-1044.

42. Chou CH & Phillips J (1992) Plasma Production Of Metallic Nanoparticles. *J. Mater. Res.* 7(8):2107-2113.

43. David B*, et al.* (2012) gamma-Fe2O3 Nanopowders Synthesized in Microwave Plasma and Extraordinarily Strong Temperature Influence on Their Mossbauer Spectra. *J. Nanosci. Nanotechnol.* 12(12):9277-9285.